Spectrum of Engineering Sciences
ISSN (e) 3007-3138 (p) 3007-312X Volume 4, Issue 3, 2026

ETM ENGINEERING AND PERFORMANCE OPTIMIZATION OF LEAD-FREE K_2GeBr_6 PEROVSKITE SOLAR CELLS

Abdul Mateen Arshad[1], Azmat Ali[*2], Ahmed Salim[3], Mohsin M. Tarar[4], SU Rahman[5], Raja Mohsin Ali Khan[6]

[1,*2,6]*Department of Physics, University of Chakwal, Chakwal, Pakistan*
[3]*Department of Electrical Engineering, NAMAL University Mianwali, Mianwali, Pakistan*
[4]*Department of Electronics Engineering, University of Chakwal, Chakwal, Pakistan*
[5]*Department of Mathematics, University of Chakwal, Chakwal, Pakistan*

[1]mateenarshad765@gmail.com, [*2]azmat.chakwal@gmail.com, [3]ahmed.salim@namal.edu.pk, [4]mohsin.tarar@uoc.edu.pk, [5]shafiq.urrahman@uoc.edu.pk, [6]mohsinkhan5252470@gmail.com

DOI: https://doi.org/10.5281/zenodo.19333001

Keywords
Perovskites, Solar Energy, lead Free, SCAPS-1D, Numerical Simulations

Article History
Received: 29 January 2026
Accepted: 12 March 2026
Published: 30 March 2026

Corresponding Author: *
Azmat Ali

Abstract
In this work, we examine a lead-free double perovskite absorber, K_2GeBr_6, in device architecture FTO/ETM/K_2GeBr_6/WoO_3/Au via SCAPS-1D simulations. A systematic comparison was conducted among three different electron transport materials (ETMs), TiO_2, SnO_2, and WO_3, with WoO_3 as the hole transport material. The results indicate that TiO_2 is the best interface with K_2GeBr_6 due to device electrical parameters such as highest efficiency of 26.8%, Voc=1.46 V, Jsc=24.9 mA/cm², and FF=73.5%. Although SnO_2 and WO_3 shows promising characteristics, such as greater recombination losses with compromised performance. The results conform TiO_2 as the most efficient ETM of K_2GeBr_6 and confer its viability as the sustainable, nontoxic absorber material in the design of the future environmentally friendly perovskite.

INTRODUCTION:

The deepening global energy crisis, combined with the environmental degradation associated with the consumption of fossil fuels, has turned the technology of renewable energy into a prime focus of scientific research[1]. Among the available renewable energy sources, solar energy is the most easily accessible and has the potential to fulfill the energy requirements of the modern world in the long run[2, 3]. With time, the solar cell technology has evolved immensely from first-generation crystalline silicon solar cells to second-generation thin-film solar cells, and now to third-generation materials. Although, silicon-based photovoltaics lead the market, their expensive processing and internal efficiency limits have initiated the search for alternative materials[4, 5]. In this regard, perovskite solar cells (PSCs) have transformed the field in a huge way, with a sudden spurt in efficiency from less than 4% in the early 2000s to more than 25% within two decades. This advance is due to the exceptional properties of perovskite absorbers, such as tunable bandgap, high optical absorption, long carrier diffusion lengths, and low-cost, simple fabrication processes [6-8].

Fig 1. Simulated diagram of K_2GeBr_6 based perovskite solar cell

Though traditional PSCs have been developing at a fast pace yet they suffer from extreme issues concerning the usage of toxic lead. Despite being highly efficient but are emvironment- and health-risky owing to the possibility of lead leakage during device operation or waste[9, 10]. Further, these materials are typically plagued by poor thermal and chemical stability, limiting their large-scale use. To overcome these limitations, researchers have focused on the field of lead-free perovskites, specifically double perovskite structures wherein the toxic Pb^{2+} is substituted with non-toxic species without sacrificing useful optoelectronic properties[11]. This approach not only removes toxicity but also enhances the device stability, thus, lead-free perovskites demonstrate a promising path towards green photovoltaics [12-14].

Fig 2. SCAPS working Procedure

Several classes of lead-free perovskites have been explored, including Bi-, Sb-, Sn-, and Cu-based materials. Antimony and bismuth-based double perovskites are stable but are plagued by indirect bandgaps and poor absorption that severely restrict the photocurrent generation. Perovskites based on tin have appropriate bandgaps but are very unstable due to the oxidation of Sn^{2+} to Sn^{4+}, which adversely affects the performance. Copper-based alternatives, though green, have deep trap states and poor carrier lifetimes, which restrict practical efficiency[15, 16].

Table 1: Material parameters of different ETMs, HTMs and Absorber.

Material parameters	TiO_2 (ETM)	WO_3 (ETM)	SnO_2 (ETM)	MoO_3 (HTM)	K_2GeBr_6 (Absorber)
Thickness(μm)	0.065	0.1	0.1	0.4	1.7
Band gap (eV)	3.2	2.6	2.6	3	1.6
Electron affinity (eV)	4.0	3.8	4.0	2.5	3.950
dielectric permittivity (relative)	10.0	4.8	9.0	12.5	3.420
CB effective density of states (cm^{-3})	1.0×10^{21}	2.2×10^{21}	2.2×10^{18}	$2.2x10^{18}$	1.0×10^{17}
VB effective density of states (cm^{-3})	2.0×10^{20}	2.2×10^{21}	1.8×10^{19}	$2.2x10^{16}$	1.0×10^{18}
electron thermal velocity (cms^{-1})	1.0×10^{7}	1.0×10^{7}	1.0×10^{7}	1.0×10^{7}	1.0×10^{7}
hole thermal velocity (cms^{-1})	1.0×10^{7}	1.0×10^{7}	1.0×10^{7}	1.0×10^{7}	1.0×10^{7}
electron mobility ($cm^2V^{-1}s^{-1}$)	2.0×10^{1}	3.0×10^{1}	1.0×10^{2}	25	1.6×10^{1}
hole mobility ($cm^2V^{-1}s^{-1}$)	1.0×10^{1}	1.0×10^{-1}	2.5×10^{1}	100	1.6×10^{1}
shallow uniform donor density ND (1/cm3)	5.0×10^{19}	6.35×10^{17}	1.0×10^{18}	0	1.0×10^{17}
shallow uniform acceptor density NA (1/cm3)	0	0	0	$1.0x10^{18}$	1.0×10^{17}

In the present work, K_2GeBr_6 has been selected as the absorber owing to its advantageous optoelectronic and structural properties, as indicated by first-principles investigations concerning Ge-based double perovskites. Germanium based double Perovskites such that K_2GeBr_6/ K_2GeI_6 have direct bandgap of 1.60/1.30 eV, which are suitable for absorption of light. These compounds also thermodynamically stable and exhibits stable structure validated by Goldschmidt tolerance factors[17]. Overall, the results of the theories verify K_2GeBr_6 as optically favorable, structurally stable, and non-toxic absorption material—and thus present an excellent candidate material for environmentally friendly high-efficiency solar cells[19, 20].

The electron hole pairs in the solar cell device is generated in absorber material by the incident of light which determines how efficient the device is? The absorber's bandgap, absorption spectrum, dielectric constants, optical conductivity, seebeck coefficient and defect tolerance govern how carriers are generated, how they recombine, and the efficiency of the solar cell. The electron transport material (ETM) plays a critical role in electron extraction, transport and in hole blocking

which reduces the recombination losses [21, 22]. The ETM is selected due to its compatibility with the absorber material. In this study three different ETMs (TiO_2, WO_3, and SnO_2) are used to determine their impact on device performance.

TiO_2 provides favorable conduction band alignment, suppresses recombination losses, and offers strong thermal and optical stability. Its compatibility with K_2GeBr_6 absorbers ensures efficient carrier extraction and consistent device performance. On the other WO_3, has a wide bandgap which support favorable band alignment and stable operation with temperatures. Its chemical stability shows long-term reliability. SnO_2 is another promising ETM, having high electron mobility, optical transparency with low-temperature processing, which enable scalable fabrication while minimizing parasitic absorption and enhancing photocurrent generation.

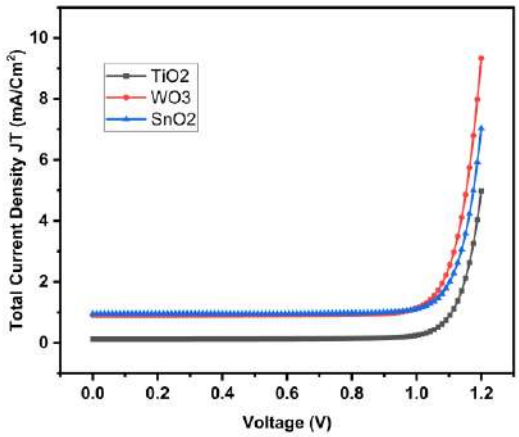

Figure 3: Total Current Density J (mA/cm^2) vs Voltage V(V) for Optimized Solar cell with different ETMS

In this study WoO_3 is used as hole transport material (HTM) due to its valence band alignment with the K_2GeBr_6 having efficient hole extraction and low recombination at the back interface. Its chemical stability and hardness shows the device as a whole for durability. Using WO_3 as hole transport material with various electron transport material (ETM), it is feasible to make a numerical comparative analysis of the relative effct of TiO_2, WO_3, and SnO_2 based device performance.

The Solar Cell Capacitance Simulator (SCAPS-1D) is used for numerical device simulations. The technique enables detailed examination of generation, recombination, current–voltage characteristics, and quantum efficiency under various structural and defect conditions [5, 22]. The results show K_2GeBr_6 with TiO_2 offer excellent efficiency and stability compared to the devices with WO_3 or SnO_2 as ETMs[23, 24]. Study of K_2GeBr_6-based solar cells with various ETMs is an important step in the direction of highly-efficient, stable, eco-friendly, nontoxic perovskite photovoltaics.

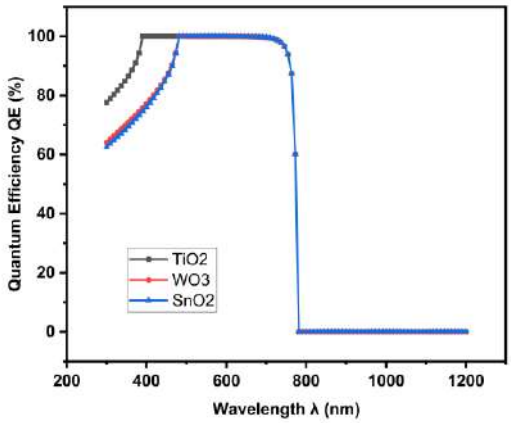

Figure 4: Quantum Efficiency QE (%) vs Wavelength (λ) of optimized solar cell with different ETMs

The non-toxic absorber with well-matched transport material presents a potential replacement for conventional solar cell. This research adds to the emerging analysis and study on lead-free perovskites, positioning K_2GeBr_6 with TiO_2 ETM and WO_3 HTM as excellent device articture. Material selection with device optimization provides scientific guidance and practical advice for realizing sustainable solar cell technologies.

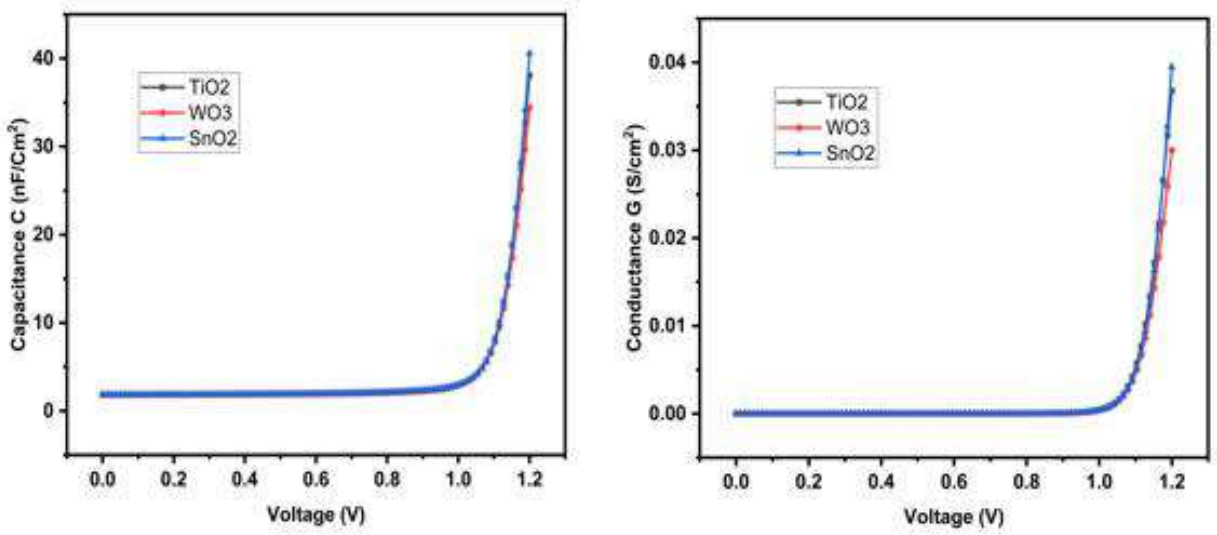

Figure 5: (a)-Capacitance and (b)-Conductance vs Voltage V(V) of optimized solar cell with different HTMs

Methodology

Numerical Simulations

The performance and effectiveness of solar cell were examined by using the SCAPS-1D (version 3.3.12) solar cell capacitance simulator, and critical device parameters were analyzed. This simulator is designed to model multi-layer solar cells and to calculated the electrical properties of device, such as open-circuit voltage (VOC), short-circuit current density (JSC), band structure, quantum efficiency (QE%), and power conversion efficiency (PCE%). SCAPS-1D relies on solving partial differential equations (PDEs), including Poisson's equation and the continuity equations for both holes and electrons.[25, 26]

$$\therefore \frac{\partial^2 \Psi}{\partial x^2} = -\frac{\partial E}{\partial x} = -\frac{\rho}{\varepsilon_x} = -\frac{\rho}{\varepsilon_x}\left[\mathbf{p} - \mathbf{n} + N_d^+ - N_a^- \pm N_{def}\right] \quad (1)$$

The symbol Ψ represents electrostatic potential, the term ε_s represents relative permittivity, 'q' represents charge, 'n' represents electrons, and 'p' represents holes. 'N_d^+' denotes donor density, 'N_a' denotes acceptor density, and 'N_{def}' represents defect density for donor/acceptor. The equation describing continuity for holes and electrons is as follows:

$$\frac{\partial_{j_P}}{\partial x} + G - U_P(n,p) = 0 \quad (2)$$

And

$$\frac{\partial_{j_n}}{\partial_x} + G - U_p(n,p) = 0 \quad (3)$$

The rates of hole recombination and electron recombination are represented by the variables $U_p(n,p)$, $U_n(n,p)$ respectively. The charge carrier generation rate, hole current density and electron current density is represented by the variable G, J_p and J_n,. The carrier current density can be obtained from these parameters:

$$j_p = qn\mu_p E - qD_p \frac{\partial p}{\partial x} \quad (4)$$

$$j_n = qn\mu_n E + qD_n \frac{\partial n}{\partial x} \quad (5)$$

The diffusion coefficients in this context are denoted as D_p and D_n, while the carrier mobilities are represented by μ_n and μ_p, with the charge denoted as q[5] . The program, developed at the University of Ghent[27], was introduced to the scientific community during the 2nd PV World Conference in Vienna for use in research and development.

Device Modeling and Analysis:

The simulated device is in the form of a planar single-junction structure made of FTO/ETM/K_2GeBr_6/WO_3/Au, where K_2GeBr_6 is the absorber, WO_3 is the hole transport material (HTM), and the electron transport material (ETM) is TiO_2, WO_3, or SnO_2 to test their effect on the performance of the device. The front contact is made up of the transparent conducting oxide FTO, and Au is the back contact. Figure 1 depicts the general structure of the proposed device, showing the sequential layering of the elements and their respective functions in transporting and collecting charges.

Numerical computation was done using SCAPS-1D[28, 29], an open-access program to simulate the electronic and optical properties of thin-film solar cells. The simulation procedure and modeling process are shown in Figure 2, and the electronic and physical properties of all materials, including bandgap, electron affinity, permittivity, mobility, doping, and defect density, are presented in Table 1. The research was conducted by comparing the performance of the three ETMs while holding the absorber and the HTM constant, hence determining their contribution to efficiency and stability improvement in K_2GeBr_6-based devices.[30]

Research Results and Discussions:

In Figure 3, At 0 V, SnO_2 (0.95 mA/cm²) and WO_3 (0.91 mA/cm²) both exhibit much higher current densities than TiO_2 (0.12 mA/cm²), which demonstrates enhanced carrier extraction. At 1.2 V, the maximum current density is achieved by WO_3 (9.33 mA/cm²), followed by SnO_2 (7.02 mA/cm²) and TiO_2 (4.98 mA/cm²). This suggests that SnO_2 performs better at low bias due to its higher electron mobility, while WO_3 performs better at high voltages due to favorable band alignment, with TiO_2 consistently lagging behind due to recombination losses[31].

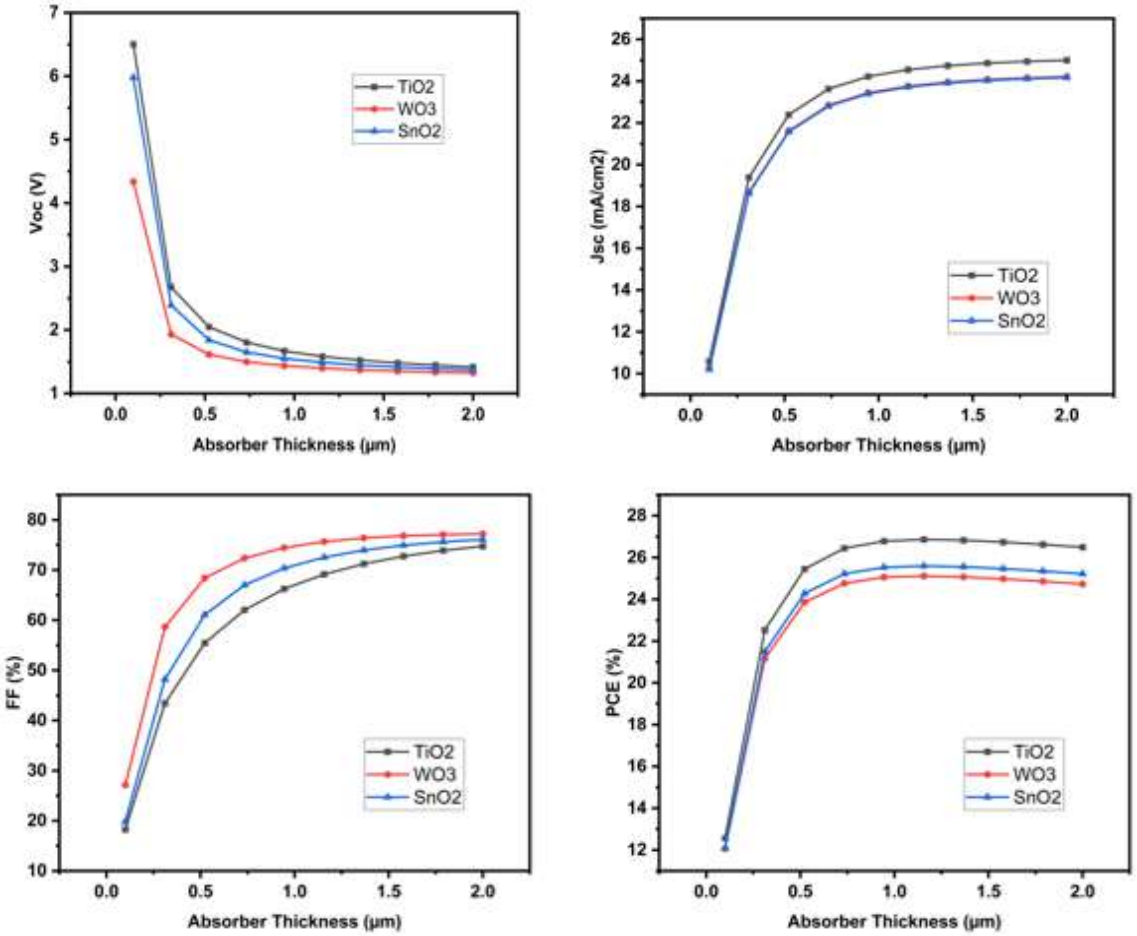

Figure 6: Variation of Electrical parameters vs Thickness of (K_2GeBr_6) absorber layer with different ETMs

In Figure 4, QE increases from 300 nm with the highest TiO_2 (77.7%) to WO_3 (64.1%) and SnO_2 (62.5%). At 390–400 nm, TiO_2 is at 100%, whereas WO_3 and SnO_2 are 76–78%. In 480–600 nm, all devices are at about 100% QE, with perfect absorption, whereas above 700 nm QE drops for all. TiO_2 performs better in the UV–visible range (300–500 nm) due to higher absorption edge, whereas WO_3 and SnO_2 are comparable in the mid-visible[32]. This verifies ETM selection primarily impacts QE at shorter wavelengths, such as comparable behavior in the flat absorption region

All the devices at 0 V possess nearly equal capacitance (TiO_2 = 1.83 nF/cm², WO_3 = 1.86 nF/cm², SnO_2 = 1.86 nF/cm²),(Figure 5), and low conductance (10^{-5} S/cm²)[33]. Capacitance and conductance increase slowly with increase in voltage up to 0.5 V, then very fast after 0.8 V, indicating improved storage and transport of charge on application of forward bias. The maximum capacitance (40.6 nF/cm²) and conductance (3.95×10^{-2} S/cm²) at 1.2 V for SnO_2 are followed by TiO_2 (38.1 nF/cm², 3.68×10^{-2} S/cm²), and the lowest capacitance (34.4 nF/cm²) and conductance (3.0×10^{-2} S/cm²) are for WO_3. It means that SnO_2 allows more efficient storage and transfer of charge, according to its higher mobility of electrons, whereas WO_3 is slow due to less efficient carrier transport. TiO_2 is average with consistent but average performance.

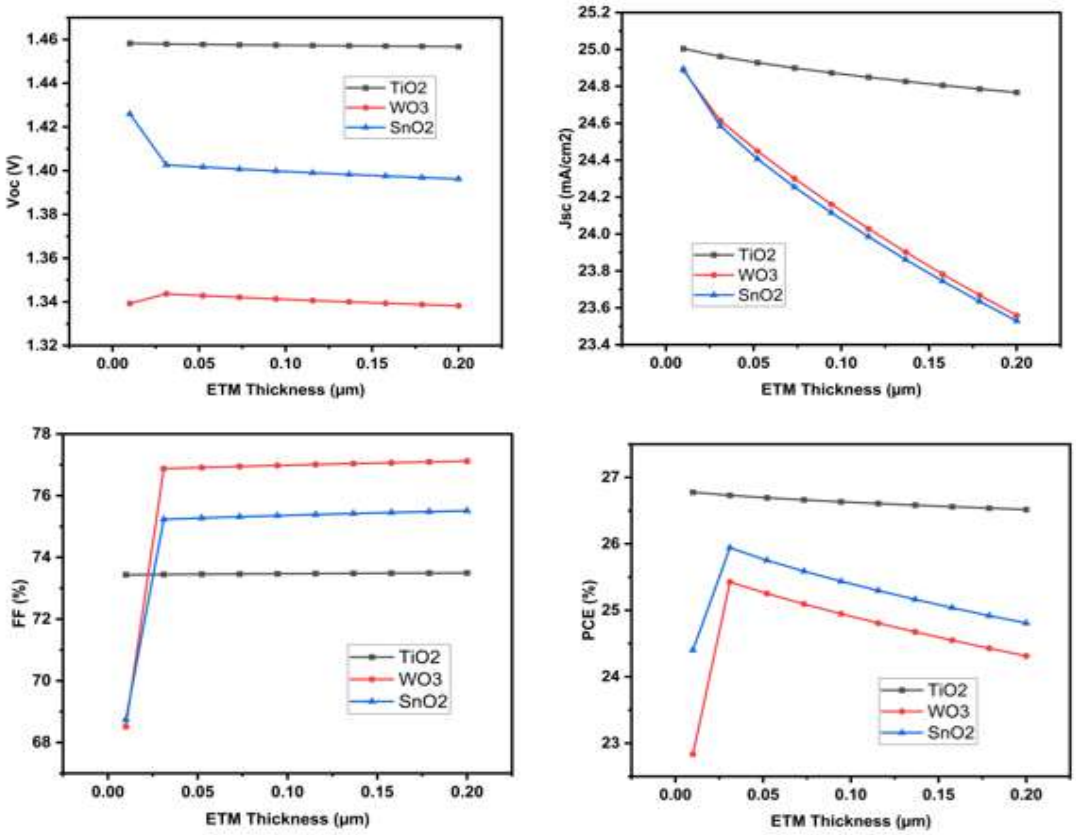

7: Variation of Electrical parameters vs Thickness of different ETMs

Figure 6 illustrates the influence of K_2GeBr_6 absorber thickness (0.1–2 μm) on TiO_2, WO_3, and SnO_2 devices. Voc decreases with greater thickness (TiO_2: 6.50 to 1.418 V, WO_3: 4.34 to 1.323 V, SnO_2: 5.98 to 1.372 V) due to greater recombination in thicker absorbers. Jsc increases very sharply in the beginning (TiO_2: 10.58 to 24.99 mA/cm², WO_3: 10.25 to 24.21 mA/cm², SnO_2: 10.21 to 24.17 mA/cm²) as more photons are absorbed and then becomes constant beyond 1.0 μm. FF increases (TiO_2: 18.26 to 74.74%, WO_3: 27.13 to 77.18%, SnO_2: 19.79 to 76.08%) as thicker absorbers enhance charge collection. PCE increases very sharply in the beginning (TiO_2: 12.56 to 26.49%, WO_3: 12.07 to 24.73%, SnO_2: 12.08 to 25.22%) and then remains constant, with TiO_2 devices being the most efficient, followed by SnO_2 and WO_3. This indicates that the optimal thickness of the absorber is a trade-off between photon absorption and recombination to achieve maximum efficiency[11]..

Figure 7 illustrates the effect of ETM thickness (0.01–0.2 μm) on TiO_2, WO_3, and SnO_2 K_2GeBr_6 devices. Voc decreases slightly with increased thickness (TiO_2: 1.458 to 1.457 V, WO_3: 1.339 to 1.338 V, SnO_2: 1.426 to 1.396 V) due to greater carrier transit length and recombination. Jsc decreases gradually too (TiO_2: 25.00 to 24.77 mA/cm², WO_3: 24.89 to 23.56 mA/cm², SnO_2: 24.89 to 23.53 mA/cm²) as thicker ETM retards electron extraction to a certain degree. FF increases slightly (TiO_2: 73.44 to 73.50%, WO_3: 68.51 to 77.12%, SnO_2: 68.73 to 75.51%) as series resistance decreases for thicker ETMs. As a result, PCE decreases slightly (TiO_2: 26.78 to 26.52%, WO_3: 22.84 to 24.31%, SnO_2: 24.40 to 24.81%), with the maximum efficiency for WO_3 devices among intermediate thickness, then SnO_2 and TiO_2[34]. This shows that ETM thickness needs to be optimized such that charge extraction and recombination are balanced for maximum efficiency.

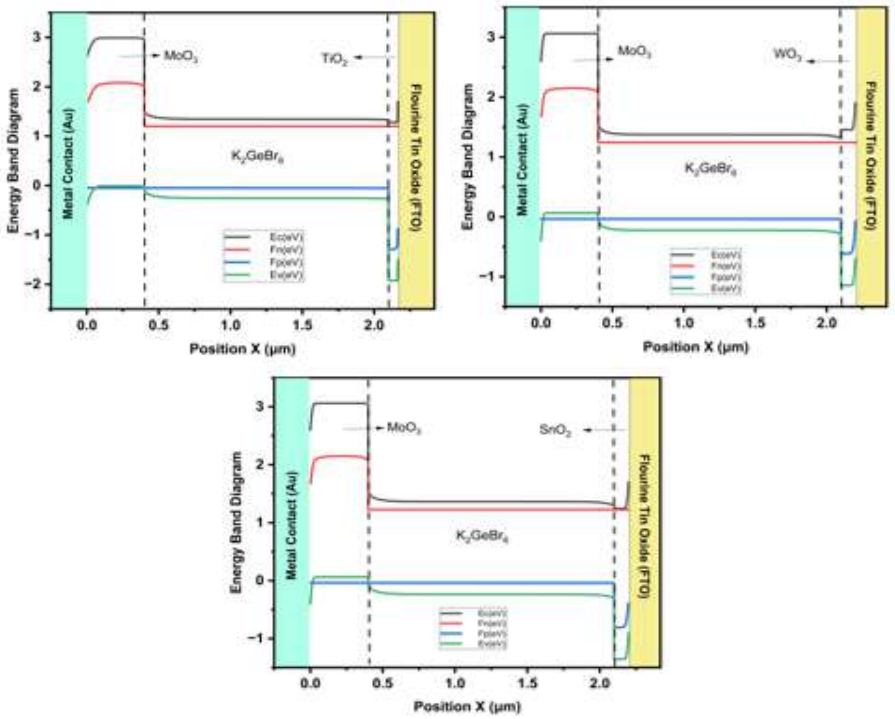

Figure 8: Energy band and layers thickness information diagram of optimized solar cell with different ETMs

In all three devices, Ec/Ev determine carrier transport and Fn/Fp splitting controls Voc.(Figure 8)[35], For the TiO_2 device, Ec at the ETL/absorber has a near-flat CBO (-2.0×10^{-4} eV) and Ev at the absorber/HTM is also aligned, but the Fn–Fp separation in the absorber is 1.251 eV, the lowest, with stronger recombination and lower Voc, as expected for TiO_2's trap-related losses. For the WO_3 device, offsets are still small (CBO ≈ -6.2×10^{-4} eV, VBO ≈ -1.4×10^{-4} eV), and Fn–Fp reaches 1.280 eV, the highest, with suppressed recombination and strongest Voc. For SnO_2, offsets are similarly flat (CBO ≈ -6.2×10^{-4} eV, VBO ≈ -1.2×10^{-4} eV) but Ec bends sharply (-1.46×10^{-2} eV/μm), increasing the built-in field and extraction, resulting in Fn–Fp of 1.264 eV, somewhat lower than WO_3 but higher than TiO_2, with stronger Jsc at little cost in Voc. Efficiency potential thus follows WO_3 > SnO_2 > TiO_2.

Figure 9 shows that an increase in defects in the absorber severely degrades device performance as it leads to higher non-radiative recombination[36]. Voc is very high at low defect density ($10^{13}cm^{-3}$). (3.83 V for TiO_2, 3.02 V for SnO_2, 2.36 V for WO_3) but drops to below 1.1 V at high density $10^{17}cm^{-3}$. Jsc is unchanged at low density (24.9 mA/cm^2) but drops to 21.4 for TiO_2, 20.4 for WO_3, and 20.5 for SnO_2 at high density, indicating weaker collection of carriers. The FF increases at moderate concentrations of defects (75%) but then steeply drops to 39–45% at high density $10^{17}cm^{-3}$. As a result, PCE drops from 29% for TiO_2 and 28% for SnO_2 and WO_3 at high density 10^{17} cm^{-3}. Generally, higher defect density reduces Voc, Jsc, FF, and PCE due to higher trap-assisted recombination, although TiO_2 shows a bit better Voc and efficiency even at high concentrations.

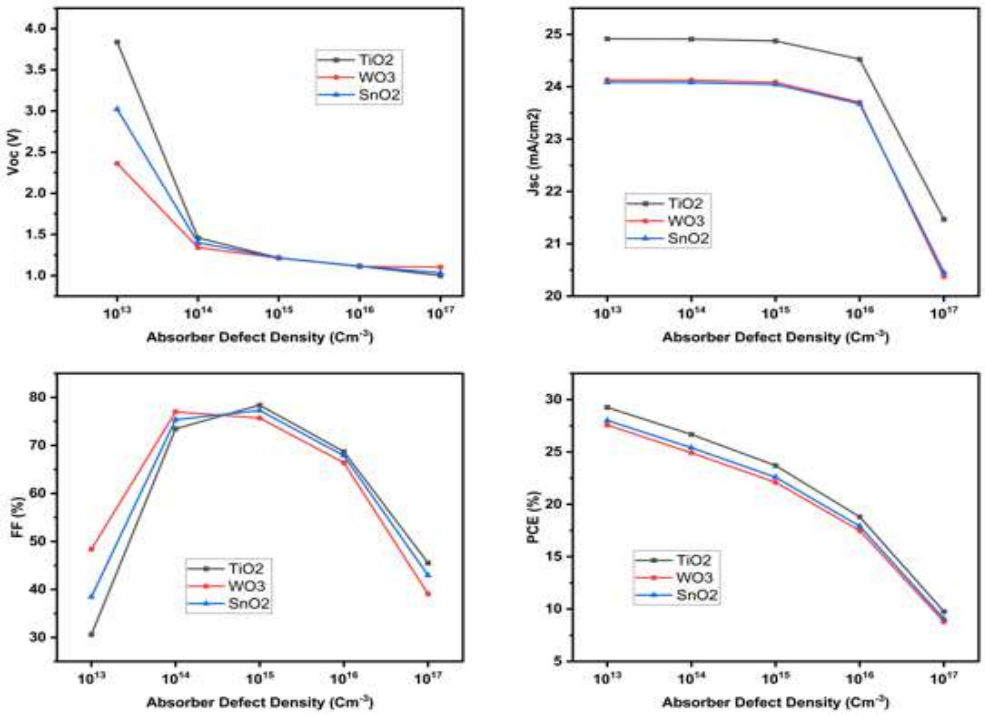

Figure 9: Variation of Electrical parameters vs Absorber Defect Density with different ETMs

In Figure 10, the depth profiles show that TiO_2 ETM yields more carrier generation (10^{21} $cm^{-3}s^{-1}$ range) than WO_3 and SnO_2 (10^{21} $cm^{-3}s^{-1}$ but consistently lower), reflecting stronger coupling of absorption and transport. While recombination for TiO_2 starts at about 10^7 $cm^{-3}s^{-1}$, its peak (1.9×10^{20} $cm^{-3}s^{-1}$) is lower than WO_3/SnO_2 (2.5×10^{20} $cm^{-3}s^{-1}$), indicating lower bulk losses. Likewise, SRH recombination in TiO_2 is lower in WO_3/SnO_2 at depth, indicating effective trap-assisted decay suppression. Thus, while with marginally greater interfacial activity, TiO_2 gives the ideal balance of high generation and controlled recombination and is hence the most efficient ETM[37].

Figure 11 illustrates As CB-DOS is raised from 1×10^{16} to 1×10^{20} cm^{-3}, Voc lowers (TiO_2: 2.06 to 1.16 V, WO_3: 1.59 to 1.15 V, SnO_2: 1.79 to 1.15 V) because of increased recombination via more available electron states (Q). Jsc is almost unchanged (24.1–24.9 mA/cm²), and FF achieves a plateau at moderate DOS (TiO_2: 79.7%, WO_3: 77.8%, SnO_2: 78.7%) and slightly falls for very high DOS. Therefore, PCE lowers (TiO_2: 28.0 to 22.5%, WO_3: 26.2 to 20.9%, SnO_2: 26.7 to 21.4%), with TiO_2 always performing better than SnO_2 and WO_3, whereby low CB-DOS restricts recombination and achieves optimal efficiency[38].

Figure 12 illustrates As VB-DOS is raised from 1×10^{16} to 1×10^{20} cm^{-3}, Voc decreases (TiO_2: 3.93 to 1.21 V, WO_3: 2.42 to 1.21 V, SnO_2: 3.15 to 1.21 V) because of increased recombination from higher hole states (Q), while Jsc is little changed (23.7–24.9 mA/cm²)[39]. FF increases dramatically at moderate DOS (TiO_2: 29.9 to 79.5%, WO3 :

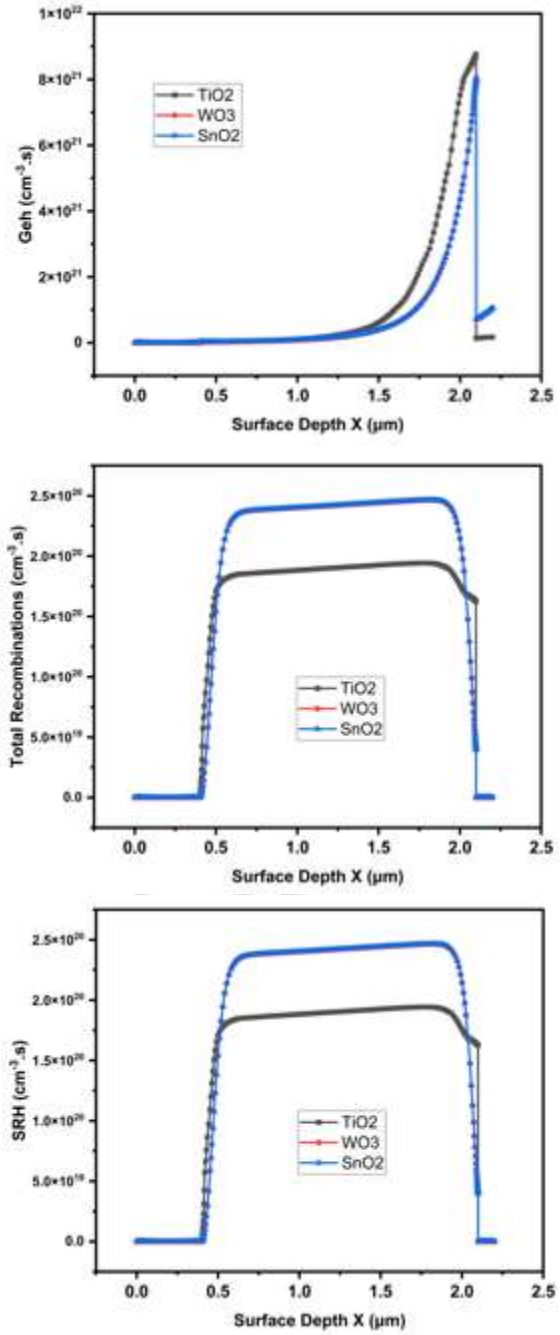

Figure 10: (a)-Generation , (b)-Total Recombination and (c)-SRH vs Surface depth of optimized solar cells with different ETMs.

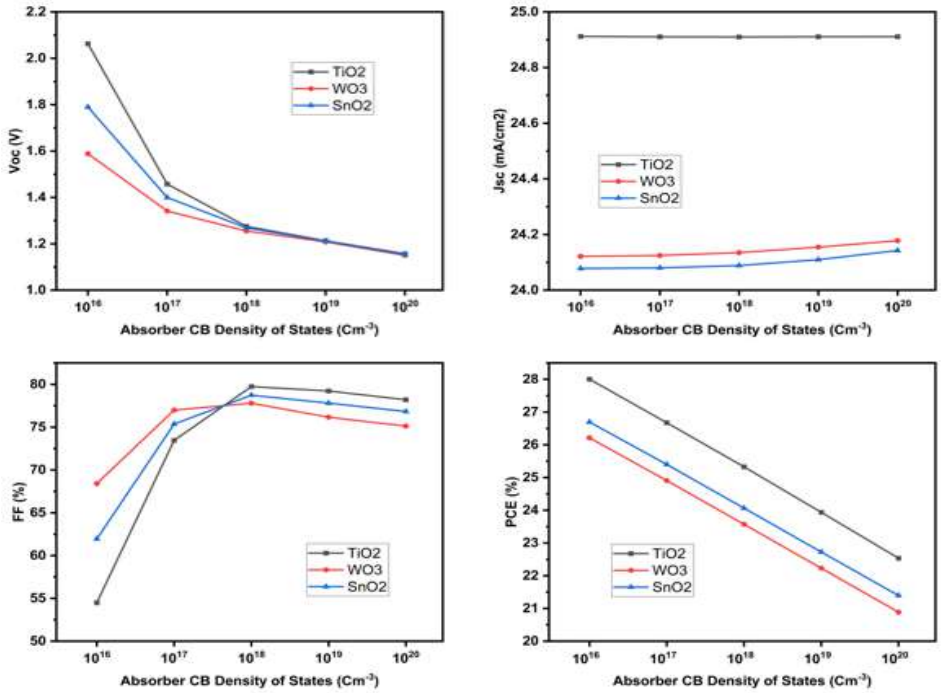

Figure 11: Variation of Electrical parameters vs Conduction band density of states (CB) of absorber layer with different ETMs

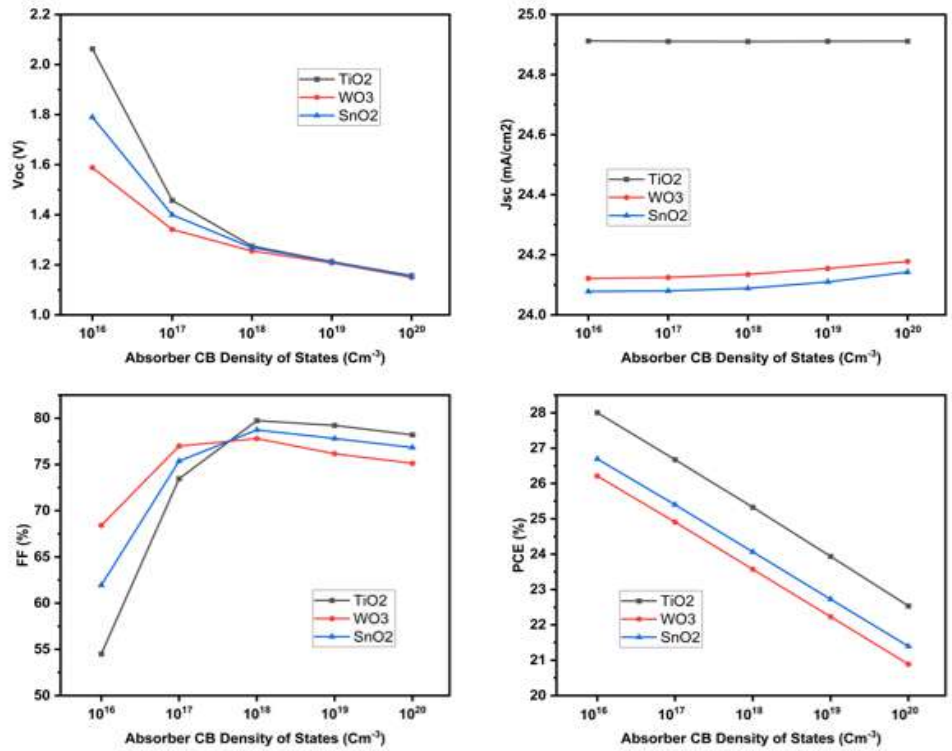

Figure 12: Variation of Electrical parameters vs Valance band density of states (VB) of absorber layer with different ETMs

47.3 to 77.8%, SnO_2: 37.0 to 78.7%) before decreasing slightly at very high DOS. As a result, PCE drops with VB-DOS (TiO_2: 29.2 to 23.9%, WO_3: 27.2 to 22.2%, SnO_2: 27.6 to 22.7%), with TiO_2 devices always outperforming SnO_2 and WO_3. This proves that low VB-DOS restricts hole-mediated recombination, maximizing efficiency, and that TiO_2 is the best ETM option for K_2GeBr_6 solar cells.

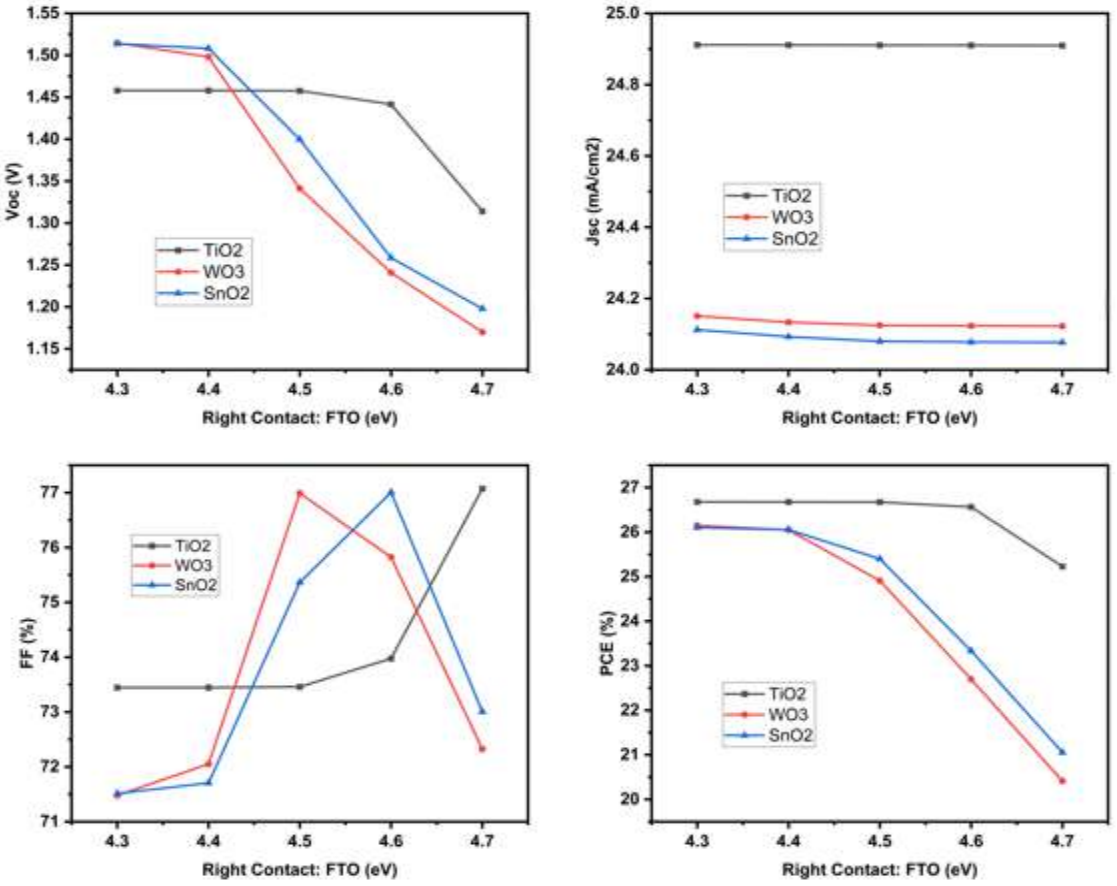

Figure 13: Variation of Electrical parameters vs Right contact (FTO) layer of optimized solar cells with different ETMs

The impact of the FTO work function (figure 13) on K_2GeBr_6 devices with TiO_2, WO_3, and SnO_2 ETMs is presented in Figure 15. By increasing FTO work function from 4.3 to 4.7 eV, Voc goes down in all devices (TiO_2: 1.458 to 1.314 V, WO_3: 1.515 to 1.170 V, SnO_2: 1.514 to 1.198 V) due to enhanced electron extraction energy barrier at the interface. Jsc is nearly constant (24.08–24.91 mA/cm²), whereas FF goes down slightly (TiO_2: 73.45 to 77.07%, WO_3: 71.48 to 72.33%, SnO_2: 71.51 to 73.01%) based on charge carrier transport balance. Therefore, PCE comes down (TiO_2: 26.68 to 25.23%, WO_3: 26.15 to 20.41%, SnO_2: 26.10 to 21.06%), and TiO_2-based cells outperform WO_3 and SnO_2 in all cases. This verifies that the best FTO work function is essential in order to minimize electron extraction barriers, suppress recombination at the contact, and achieve maximum efficiency[41].

Figure 14 illustrates the influence of Au metal work function on K_2GeBr_6 devices with TiO_2, WO_3, and SnO_2 ETMs. With varying Au work function from 5.1 to 5.5 eV, Voc increases (TiO_2: 1.458 to 1.920 V, WO_3: 1.341 to 1.461 V, SnO_2:

1.400 to 1.613 V) owing to better matching with the absorber, better hole extraction, and reduced interfacial recombination. Jsc is theoretically unaffected (24.08–24.91 mA/cm²), whereas FF decreases slightly in the case of TiO_2 (73.46 to 58.44%) but is excellent in the case of WO_3 (76.99 to 73.50%) and SnO_2 (75.36 to 67.96%) according to charge transport balance. PCE then improves (TiO_2: 26.67 to 27.95%, WO_3: 24.91 to 25.91%, SnO_2: 25.40 to 26.39%), with the maximum efficiency being delivered by TiO_2 devices followed by SnO_2 and WO_3. This clearly shows that optimal Au work function improves hole extraction, reduces recombination at the back contact, and also maximizes device performance in general[42].

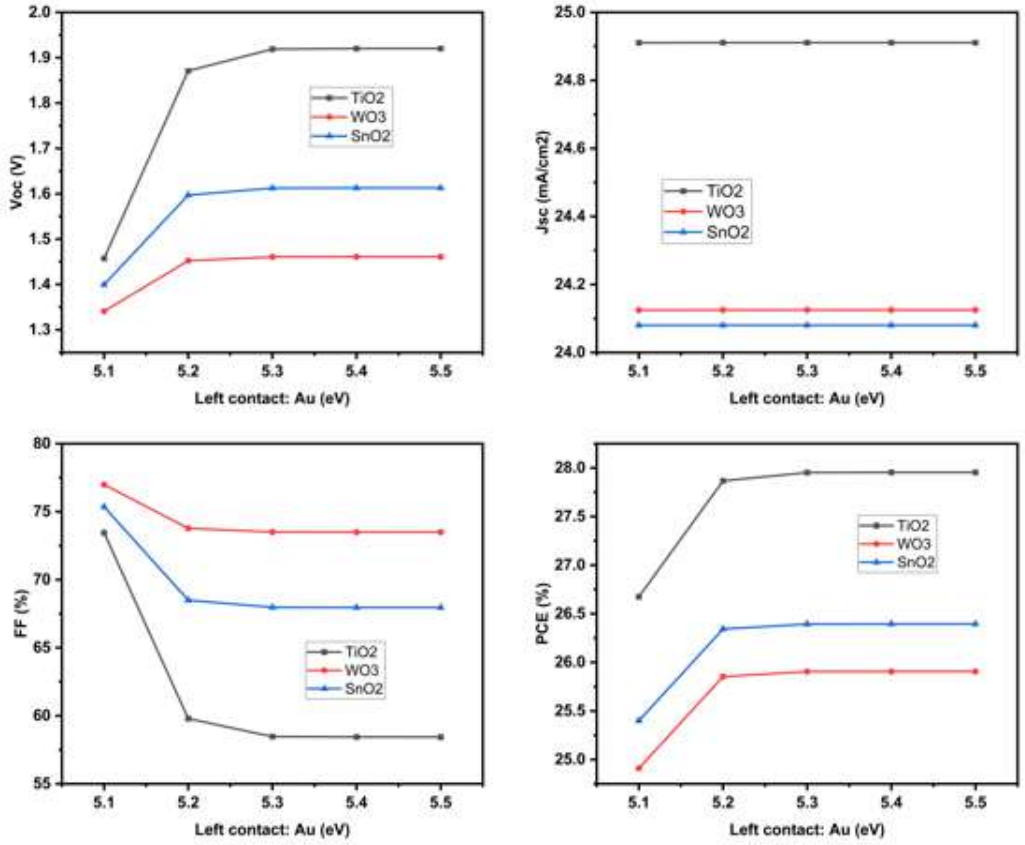

Figure 14: Variation of Electrical parameters vs Left contact (Au) layer of optimized solar cells with different ETMs

Figure 15 illustrates the influence of temperature (260–360 K) on K_2GeBr_6 devices with TiO_2, WO_3, and SnO_2 ETMs. Voc decreases with increasing temperature (TiO_2: 1.475 to 1.296 V, WO_3: 1.249 to 1.294 V, SnO_2: 1.294 to 1.295 V) because of increased carrier recombination and lower built-in potential at elevated temperatures. Jsc is comparatively stable (24.07–24.91 mA/cm²), while FF increases slightly (TiO_2: 73.60 to 78.31%, WO_3: 77.24 to 78.56%, SnO_2: 78.56 to 78.55%) with decreased series resistance. PCE decreases accordingly (TiO_2: 27.04 to 25.28%, WO_3: 23.29 to 24.52%, SnO_2: 24.52 to 24.49%), with TiO_2 devices being the most efficient at low temperatures, followed by SnO_2 and WO_3. This indicates that higher temperature increases recombination, decreasing Voc and overall efficiency, but FF increases slightly due to lower resistance effects [43].

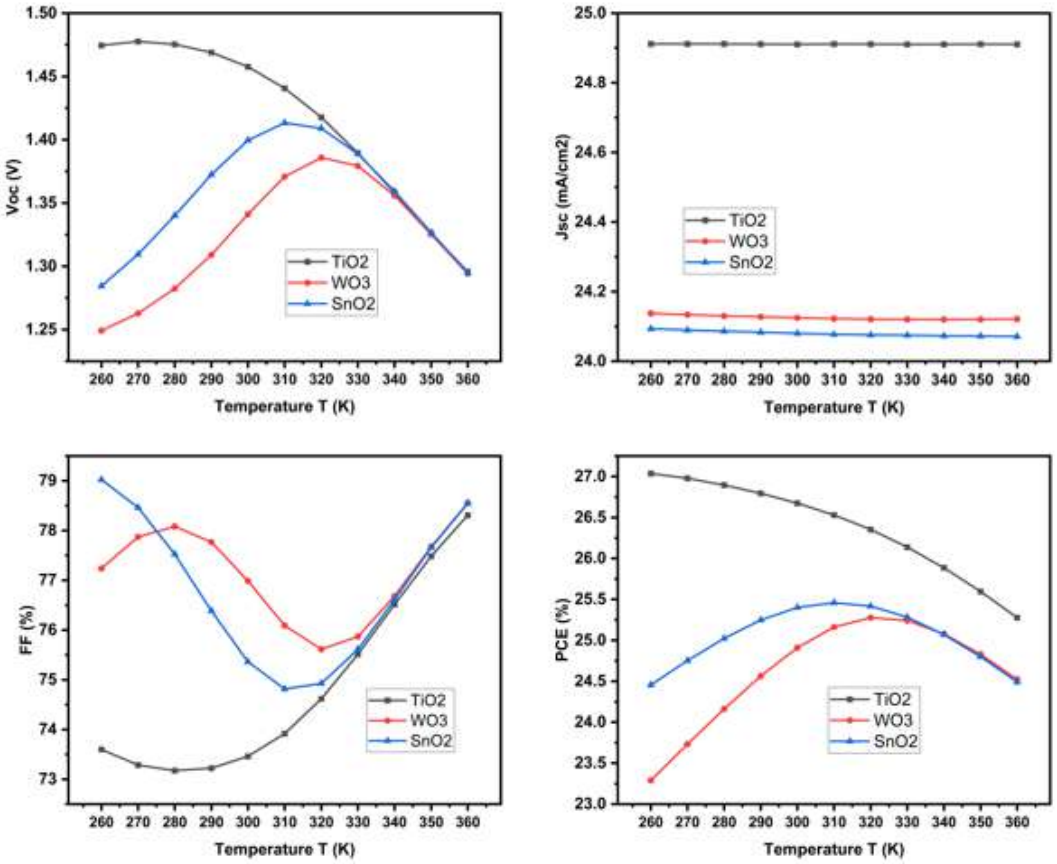

Figure 15: Variation of Electrical parameters vs Temperature of devices with different ETMs

Table 2: Solar cell device architecture vs optimized electrical parameters

Device Structure	Voc (V)	Jsc (mA/cm2)	FF (%)	PCE (%)
FTO/WoO_3/K_2GeBr_6/TiO_2/Au	1.4576	24.9106	73.46	26.67
FTO/WoO_3/K_2GeBr_6/WO_3/Au	1.3411	24.1247	76.99	24.91
FTO/WoO_3/K_2GeBr_6/SnO_2/Au	1.3996	24.0801	75.36	25.40

Conclusion:

Solar cell device level simulations of lead free K_2GeBr_6 absorber with TiO_2, WO_3, and SnO_2 electron transport materials shows that TiO_2 is the best ETM with the highest carrier generation rate (10^{21} $cm^{-3}s^{-1}$), lowest recombination loss (1.9×10^{20} $cm^{-3}s^{-1}$ as compared to 2.5×10^{20} $cm^{-3}s^{-1}$ for WO_3/SnO_2), and consistently better photovoltaic performance, with device electric characteristics (PCE % ≈ 23–27%, Voc ≈ 1.3–1.46 V, Jsc ≈ 24 mA/cm², FF ≈ 73–77%). The K_2GeBr_6 is good absorbance performance, at an optimized thickness of 1 µm achieving a strong balance between the absorption of photons and recombination. The defect densities greater than 10^{16} cm^{-3} reduce efficiency, which underline the significance of interface and bulk defect

passivation. Overall, this study shows that TiO_2/K_2GeBr_6 architecture as a high-efficiency and stable device combination, offering a sustainable alternative to lead-based perovskites and a strong foundation for the development of next-generation, eco-friendly solar cells.

REFERENCES

1. Glaser, P.E., *Power from the sun: Its future.* Science, 1968. **162**(3856): p. 857-861.
2. Hossain, M.K., et al., *Current applications and future potential of rare earth oxides in sustainable nuclear, radiation, and energy devices: a review.* ACS Applied Electronic Materials, 2022. **4**(7): p. 3327-3353.
3. Li, X., et al., *Advancing energy sustainability through solar-to-fuel technologies: From materials to devices and systems.* Small Methods, 2024. **8**(11): p. 2400683.
4. Hasan, S.A.U., et al., *Stability challenges for a highly efficient Perovskite/Silicon Tandem Solar cell: A review.* Solar RRL, 2024. **8**(6): p. 2300967.
5. ul Abdin, Z., et al., *Numerical modelling analysis of (FA) 0.85 Cs0. 15Pb (I0. 85 Br0. 15) 3:(FAPI)-based perovskite solar cell with different ETMs using solar capacitance simulator.* Solar Energy, 2021. **228**: p. 100-119.
6. Shiyu, Q., et al., *Toxicity of cadmium and its competition with mineral nutrients for uptake by plants: A review.* Pedosphere, 2020. **30**(2): p. 168-180.
7. Kumar, P., et al., *Research progress and challenges in extending the infra-red absorption of perovskite tandem solar cells.* Nano Energy, 2024. **121**: p. 109175.
8. Yin, W.-J., et al., *Halide perovskite materials for solar cells: a theoretical review.* Journal of Materials Chemistry A, 2015. **3**(17): p. 8926-8942.
9. Guin, M. and R. Singh, *Lead-Free Perovskite Solar Cells.* Perovskite based Materials for Energy Storage Devices, 2023. **151**: p. 111-154.
10. Zhang, Y., et al., *Halide perovskite for enhancing photocatalytic efficiency: basic characteristics, nanostructure engineering and applications.* Journal of Materials Chemistry A, 2024. **12**(31): p. 19757-19782.
11. Jiang, X., et al., *Tin halide perovskite solar cells: an emerging thin-film photovoltaic technology.* Accounts of Materials Research, 2021. **2**(4): p. 210-219.
12. de Souza Carvalho, T.A., et al., *Lead-free metal halide perovskite nanocrystals: from fundamentals to applications.* Chemistry–A European Journal, 2023. **29**(4): p. e202202518.
13. Gao, P., M. Grätzel, and M.K. Nazeeruddin, *Organohalide lead perovskites for photovoltaic applications.* Energy & Environmental Science, 2014. **7**(8): p. 2448-2463.
14. Jena, A.K., A. Kulkarni, and T. Miyasaka, *Halide perovskite photovoltaics: background, status, and future prospects.* Chemical reviews, 2019. **119**(5): p. 3036-3103.
15. Zhang, Z., et al., *Mechanistic understanding of oxidation of tin-based perovskite solar cells and mitigation strategies.* Angewandte Chemie International Edition, 2023. **62**(45): p. e202308093.
16. Kojima, A., et al., *Organometal halide perovskites as visible-light sensitizers for photovoltaic cells.* Journal of the american chemical society, 2009. **131**(17): p. 6050-6051.
17. Al-Muhimeed, T.I., et al., *New lead-free double perovskites X2GeI6 (X= K, Rb, Cs) for solar cells, and renewable energy as an alternate of hybrid perovskites.* International Journal of Energy Research, 2021. **45**(13): p. 19645-19652.
18. Bouferrache, K., et al., *Organic–inorganic hexahalometalate-crystal semiconductor K 2 (Sn, Se, Te) Br 6 hybrid double perovskites for solar energy applications.* RSC advances, 2025. **15**(15): p. 11923-11933.

19. Ali, A., et al., *First-principles calculations of mechanical, optoelectronic, and thermal properties of double perovskite K2GeCl/Br6 for solar cell applications.* Journal of Physics and Chemistry of Solids, 2021. **159**: p. 110295.
20. Behera, D. and S.K. Mukherjee, *Structural, elastic, electronic and thermoelectric properties of K2GeBr6: A first principle approach.* Materials Today: Proceedings, 2023.
21. Sun, H., et al., *Optoelectronic synapses based on a triple cation perovskite and Al/MoO 3 interface for neuromorphic information processing.* Nanoscale Advances, 2024. **6**(2): p. 559-569.
22. Mamoun, S., A.E.-H. Merad, and A. Benmansour, *Simulation study of electronic band diagram engineering and electrical parameters to boost the photovoltaic performance of novel Rb2PtI6 double perovskite solar cell.* The Eurasia Proceedings of Science Technology Engineering and Mathematics, 2024. **32**: p. 389-399.
23. Otoufi, M.K. and A. Kermanpur, *Improved electron transport in planar perovskite solar cells using TiO2, SnO2 and WO3 ultra-thin layers: a comparison on all single layer and bilayer structures.* Bulletin of Materials Science, 2024. **47**(3): p. 217.
24. Mujtaba, A., et al., *Enhancing perovskite solar cell efficiency: ZnO–WO 3 as an electron transport layer to minimize recombination losses.* RSC advances, 2025. **15**(31): p. 25019-25029.
25. Das, U., et al. *Numerical Investigation of Lead-Free CH 3 NH 3 SnI 3 Perovskite Solar Cell for Photovoltaic Performance Improvement using SCAPS-1D.* in *2024 International Conference on Advances in Computing, Communication, Electrical, and Smart Systems (iCACCESS).* 2024. IEEE.
26. Salih, M.A., M.A. Mustafa, and B.A. Yousef, *Developing lead-free perovskite-based solar cells with planar structure in confined mode arrangement using SCAPS-1D.* Sustainability, 2023. **15**(2): p. 1607.
27. Bhattarai, S. and T. Das, *Optimization of carrier transport materials for the performance enhancement of the MAGeI3 based perovskite solar cell.* Solar Energy, 2021. **217**: p. 200-207.
28. Hossain, M.K., et al., *Effect of various electron and hole transport layers on the performance of CsPbI3-based perovskite solar cells: a numerical investigation in DFT, SCAPS-1D, and wxAMPS frameworks.* ACS omega, 2022. **7**(47): p. 43210-43230.
29. Rubel, M., et al., *First-principles calculations to investigate structural, elastic, electronic, thermodynamic, and thermoelectric properties of CaPd3B4O12 (B= Ti, V) perovskites.* Results in Physics, 2022. **42**: p. 105977.
30. Rubel, M., et al., *First-principles calculations to investigate physical properties of single-cubic (Ba0. 82K0. 18)(Bi0. 53Pb0. 47) O3 novel perovskite superconductor.* Materials Today Communications, 2022. **33**: p. 104302.
31. Saliba, M. and L. Etgar, *Current density mismatch in perovskite solar cells.* ACS Energy Letters, 2020. **5**(9): p. 2886-2888.
32. Dharmadasa, I., et al., *Perovskite solar cells: a deep analysis using current–voltage and capacitance–voltage techniques.* Journal of materials science: Materials in electronics, 2019. **30**(2): p. 1227-1235.
33. Zhou, S., et al., *Insight into the structural, optical and mechanical properties of RbSnX3 (X= Cl, Br, I) under high pressure.* The Journal of Physical Chemistry C, 2023. **127**(27): p. 13346-13355.
34. Ouma, C.N., et al. *In silico insights into the tunable magnetic properties of transition metal doped monolayer SnS2.* in *2018 Open Innovations Conference (OI).* 2018. IEEE.
35. Saadat, M. and S. Bameri, *Comprehensive analysis of transport layers and interface defects in MAPbI3 based PSCs for enhanced efficiency.* Discover Applied Sciences, 2025. **7**(5): p. 440.
36. Chowdhury, M., et al., *Effect of deep-level defect density of the absorber layer and n/i interface in perovskite solar cells by SCAPS-1D.* Results in Physics, 2020. **16**: p. 102839.

37. Schuster, J., et al., *Junction optimization in HgCdTe: Shockley-Read-Hall generation-recombination suppression.* Applied Physics Letters, 2015. **107**(2).
38. Chen, R. and C. Persson, *Band-edge density-of-states and carrier concentrations in intrinsic and p-type CuIn1− xGaxSe2.* Journal of Applied Physics, 2012. **112**(10).
39. Vasheghani Farahani, S., et al., *Valence-band density of states and surface electron accumulation in epitaxial SnO 2 films.* Physical Review B, 2014. **90**(15): p. 155413.
40. Shieh, J.-T., et al., *The effect of carrier mobility in organic solar cells.* Journal of Applied Physics, 2010. **107**(8).
41. Ali, M.F. and M.F. Hossain, *Influence of Front and Back Contacts on Photovoltaic Performances of p-n Homojunction Si Solar Cell: Considering an Electron-Blocking Layer.* International Journal of Photoenergy, 2017. **2017**(1): p. 7415851.
42. Minemoto, T. and M. Murata, *Impact of work function of back contact of perovskite solar cells without hole transport material analyzed by device simulation.* Current Applied Physics, 2014. **14**(11): p. 1428-1433.
43. Singh, P. and N.M. Ravindra, *Temperature dependence of solar cell performance—an analysis.* Solar energy materials and solar cells, 2012. **101**: p. 36-45.